SANDIA REPORT

SAND2001-8518
Unlimited Release
Printed September 2001

Corrosion Resistance of Stainless Steels During Thermal Cycling in Alkali Nitrate Molten Salts

R. W. Bradshaw, S. H. Goods

Prepared by
Sandia National Laboratories
Albuquerque, New Mexico 87185 and Livermore, California 94550

Sandia is a multiprogram laboratory operated by Sandia Corporation, a Lockheed Martin Company, for the United States Department of Energy under Contract DE-AC04-94AL85000.

Issued by Sandia National Laboratories, operated for the United States Department of Energy by Sandia Corporation.

Available to DOE and DOE contractors from
U.S. Department of Energy
Office of Scientific and Technical Information
P.O. Box 62
Oak Ridge, TN 37831

Telephone:(865)576-8401
Facsimile:(865)576-5728
E-Mail: reports@adonis.osti.gov
Online ordering: http://www.doe.gov/bridge

Available to the public from
U.S. Department of Commerce
National Technical Information Service
5285 Port Royal Rd
Springfield, VA 22161

Telephone:(800)553-6847
Facsimile:(703)605-6900
E-Mail: orders@ntis.fedworld.gov
Online order: http://www.ntis.gov/ordering.htm

SAND 2001-8518
Unlimited Release
Printed August 2001

CORROSION RESISTANCE OF STAINLESS STEELS DURING THERMAL CYCLING IN ALKALI NITRATE MOLTEN SALTS

R. W. Bradshaw
Materials Chemistry Department

S. H. Goods
Materials Mechanics Department
Sandia National Laboratories/CA

ABSTRACT

The corrosion behavior of three austenitic stainless steels was evaluated during thermal cycling in molten salt mixtures consisting of $NaNO_3$ and KNO_3. Corrosion tests were conducted with Types 316, 316L and 304 stainless steels for more than 4000 hours and 500 thermal cycles at a maximum temperature of 565°C. Corrosion rates were determined by chemically descaling coupons. Metal losses ranged from 5 to 16 microns and thermal cycling resulted in moderately higher corrosion rates compared to isothermal conditions. Type 316 SS was somewhat more corrosion resistant than Type 304 SS in these tests. The effect of carbon content on corrosion resistance was small, as 316L SS corroded only slightly slower than 316 SS. The corrosion rates increased as the dissolved chloride content of the molten salt mixtures increased. Chloride concentrations approximating 1 wt.%, coupled with thermal cycling, resulted in linear weight loss kinetics, rather than parabolic kinetics, which described corrosion rates for all other conditions. Optical microscopy and electron microprobe analysis revealed that the corrosion products consisted of iron-chromium spinel, magnetite, and sodium ferrite, organized as separate layers. Microanalysis of the elemental composition of the corrosion products further demonstrated that the chromium content of the iron-chromium spinel layer was relatively high for conditions in which parabolic kinetics were observed. However, linear kinetics were observed when the spinel layer contained relatively little chromium.

ACKNOWLEDGMENTS

The authors gratefully acknowledge the important contributions to this study made by a number of Sandians; Andy Gardea (8723) for metallography, Bernie Bernal (8816), Chris Rood and Nancy Yang (8723) for scanning electron microscopy and electron microprobe analysis, Dale Boehme (formerly 8355) for X-ray diffraction analysis, and Sam Dunkin (formerly 6216) for constructing and operating the experimental apparatus.

This work was supported by the U. S. Dept. of Energy under contract DE-AC04-94AL85000.

Table of Contents

Page

This page intentionally left blank.

Corrosion Resistance of Stainless Steels During Thermal Cycling in Alkali Nitrate Molten Salts

I. Introduction

This report examines the corrosion behavior of some of the primary containment materials that were used to construct Solar Two, a solar central receiver (SCR) power demonstration plant.[1,2] This technology demonstration was conducted jointly by a consortium of electric power utility companies and the U. S. Department of Energy. In an SCR system, sunlight is focused by an array of computer-controlled mirrors onto a 'receiver', a structure comprised of tubing through which a heat transfer fluid circulates. The heat transfer fluid chosen for Solar Two was a molten salt consisting of 60 wt. % $NaNO_3$ and 40 wt.% KNO_3, which has a melting point of approximately 238°C and an intended working range of 290°C to 570°C. The molten salt is also used to store thermal energy as sensible heat, thereby allowing the peak power production to coincide with peak demand.[1] The proportions of the individual nitrates were chosen to minimize the cost of the resulting mixture, while providing good physical properties of the molten salt.

Type 316 SS was used to construct the receiver in the Solar Two system while Type 304 SS was used for the hot salt storage tank and piping. These stainless steels were chosen because previous laboratory work showed that they exhibit good corrosion resistance during isothermal crucible experiments. These previous tests were conducted at 570°C and the extent of corrosion was measured from descaled weight losses. The total metal losses of 316SS and 304SS were about 10 microns after 7,000 hours of exposure.[3] Other corrosion experiments were performed using low-velocity flow loops in which coupons were exposed to the molten salt at approximately 590°C. Under these conditions, corrosion of 304SS consumed about 8 microns after 4200 hours.[4] Corrosion data obtained from a molten salt pipe loop pumped at a relatively large flow rate agreed with these results and further demonstrated the adequate corrosion in molten resistance of 316SS and 304SS.[5] In addition to good corrosion resistance, no degradation of mechanical properties occurred after long-term isothermal exposure to molten nitrate salt.[6]

Of all the components in an SCR system, the receiver tubes encounter the most demanding environment with regard to mechanical and thermal stress. Due to the diurnal nature of SCR operation, the receiver must tolerate many excursions between its maximum operating temperature and the ambient temperature. However, other components that contain molten salt at the maximum operating temperature, such as hot-salt piping, superheater, also experience thermal cycling, though to a lesser degree. Thermal cycling generally aggravates high temperature oxidation, but the degree to which a particular material may be affected in any given environment is difficult to predict.[7,8] The primary effect of thermal cycling on corrosion is to damage protective surface oxide layers mechanically, thereby compromising the barrier to corrosion such layers provide. Thermal cycling can cause oxide layers to fail either adhesively (due to the different thermal expansion coefficients of the oxide and the metal substrate) or cohesively (due to tensile stress gradients within the oxide layer upon rapid cooling).

The only prior work concerning the effect of thermal cycling on corrosion Fe-Cr-Ni alloys nitrate salts of which we are aware describes the metallographic examination of Incoloy® 800 tubing (Inco Alloys International, Inc., Huntington, WV, nominally Fe-20Cr-35Ni) removed from a prototype SCR test facility.[9] This tubing had experienced almost 1000 hours of operation at temperatures as high as 565°C and had undergone several hundred thermal cycles. Microscopic inspection of tubing sections from this facility revealed that the surfaces exposed to molten salt were covered with an adherent oxide layer about 20 microns thick. Corrosion of Incoloy 800 has also been studied at constant temperature in a thermal convection loop.[10] Coupons exposed at the same temperature as above displayed only half as much scale formation after 5000 hours. This contrast in scale formation suggests that thermal cycling may significantly affect corrosion rates relative to isothermal exposure.

In addition to thermal cycling, corrosion may also be influenced by the presence of certain impurities in the molten salt. The impurities typically present in commodity grades of nitrates are NaCl, $KClO_4$, Na_2SO_4, and alkalinity. Of these impurities, chloride may be a concern because it is often found to accelerate corrosion in high temperature oxidizing environments.[11] Typically, the lower-cost grades of nitrate salts tend to have higher impurity concentrations, thus it is necessary to evaluate the impact on such secondary constituents on corrosion when assessing cost trade-offs for a large SCR system. A previous corrosion study of both stainless and carbon steels showed only a moderate effect of dissolved chlorides on corrosion.[3] However, thermal cycling and impurities in the molten salt may act in concert to increase corrosion rates as chloride often degrades adhesion of thermally-grown oxides on high temperature alloys.[11,12]

The scope of the present study was to examine the effect of thermal cycling on corrosion of several 300-series stainless steels in molten nitrate salts. We investigated 316 SS, 316L SS (a low-carbon version of 316 SS), and 304 SS. The test protocol was designed to generate data on corrosion rates during relatively long-term tests to allow extrapolation to the expected service lifetime of SCR power systems (20 to 30 years, comparable to conventional power plants). The thermal cycle and temperature limits were chosen to mimic the expected operating conditions of the Solar Two receiver. We also evaluated the effect that chloride, a minor impurity in the nitrate salts, has on corrosion during thermal cycling. These corrosion data are compared with isothermal corrosion data generated during the current tests, as well as from prior experiments. The study included microscopic examination of the elemental composition of the corrosion products to determine whether a clear correlation existed between the corrosion products and corrosion kinetics. The goal of this effort was to develop a diagnostic basis for evaluating metallurgical samples removed from operating plants and, thereby, a means for predicting the remaining service life.

II. Expermental

Alloy coupons

The elemental compositions of the heats of 316 SS, 316L SS, and 304 SS used to prepare corrosion samples are shown in Table I. Rectangular coupons measuring approximately 20 mm x 50 mm x 2 mm in thickness were fabricated by Metal Samples Co., Inc., Munford, AL. The coupons were ground with 120 grit carborundum paper to produce uniform surface finishes.

TABLE I. Elemental compositions of stainless steels tested (wt. % by analysis)

Alloy	Fe	C	Cr	Ni	Mo	Si	Mn
316 SS	Bal.	0.06	16.93	10.10	2.20	0.49	1.51
316L SS	Bal.	0.017	16.19	10.19	2.10	0.39	1.72
304 SS	Bal.	0.06	18.30	8.07	-	0.42	1.85

Molten salt mixtures

Four binary nitrate mixtures having the same nominal composition of 60% (wt.) $NaNO_3$ and 40% KNO_3 were used for corrosion testing. The sources of the constituent nitrates in these mixtures are identified in Table II. Mixtures M-1 and M-2 are commercial sources of relatively high purity salt. Mixture M-3 is a commercially available nitrate containing somewhat higher impurity concentrations. Mixture M-4 was comprised of the same salt as M-1 but NaCl was deliberately added to a concentration of 1.3 wt.%. This resulted in about 30% more chloride ion than the highest level expected in any commercial grade of salt. The intent of using mixtures M-1 and M-4 was to examine the effect of chloride concentration on corrosion in the absence of significant amounts of other impurities.

The initial concentrations of some of the principal impurities in the nitrate mixtures used for the experiments are shown in Table II. These values were determined using standard chemical analysis techniques. As dissolved chloride may not be the only impurity influencing the corrosion characteristics of the alloys studied, other potentially important impurities in the nitrate mixtures, including perchlorate, sulfate, and carbonate are listed. We also list the values for total chloride, as the perchlorate present initially is converted to a stoichiometrically equivalent amount of chloride during the first several hundred hours of the tests.[3] Samples of the molten salt were periodically withdrawn from each crucible and analyzed to determine if any changes occurred in the minor constituents. We observed no changes in composition other than the expected formation of approximately 3 wt.% nitrite (NO_2-) resulting from equilibrium dissociation of nitrate.[13]

TABLE II. Sources of the constituent nitrate salts and the initial concentrations of impurities (wt.%) of the salt mixtures used for the corrosion tests.

Constituent	Molten Salt Mixture			
	M-1	M-2	M-3	M-4‡
$NaNO_3$ (source)	Coastal†	Chilean* (Technical)	Chilean (Industrial)	Coastal
KNO_3 (source)	Coastal	Cedar Chemical§	Chilean	Coastal
Chloride	0.040	0.060	0.462	0.760
Perchlorate	0.035	0.064	0.316	0.045
Total Chloride	**0.05**	**0.07**	**0.55**	**0.82**
Sulfate	<.002	0.011	0.182	<.002
Carbonate	0.010	0.010	0.021	0.006

† Coastal Chemical Co., Inc., Houston, TX

* Chilean Nitrate Corp., Norfolk, VA

§ Cedar Chemical Co., Vicksburg, MS

‡ 1.3 wt.% NaCl was added to M-1 to formulate mixture M-4.

Testing procedure

The stainless steel coupons were immersed in crucibles constructed of 304 SS that contained about 10 kg of the nitrate mixtures. The maximum crucible temperature was controlled to ±5°C. The corrosion coupons were fastened to a fixture that was raised and lowered into the crucibles containing molten salt as controlled by an automatic timer. The fixtures for all four crucibles were driven by a pneumatic cylinder attached to a common rack. A photograph of the apparatus is shown in Figure 1. The periodic temperature cycle was chosen to achieve a balance between significant growth of corrosion products, which requires prolonged aging at the maximum temperature, and the number of thermal cycles obtainable in a reasonable testing time. The cycling period also required adequate time for cooling of the samples and the fixture caused by free convection in air at ambient temperature. We chose a temperature program resembling the intended daily service conditions of a receiver; 7.5 hours at the maximum temperature and 0.5 hours cooling in ambient air, for a total cycle time of 8 hours. This schedule allowed three cycles to be run daily. The temperature/time profile used for the thermal cycling tests is shown in Figure 2 and consisted of a 7.5 hour interval in which the coupons were immersed at the maximum temperature of 565°C (1050°F). At the end of the immersion period, the coupons were raised above their respective crucibles and cooled in air for 15 minutes, attaining a temperature of about 95°C (200°F). The coupon racks were then lowered to an intermediate position, a few inches above the melts, to allow pre-heating for another 15 minutes to about 200°C-250°C. The intent of this stage was to avoid thermal shock effects when the coupons were lowered in the molten salt. Such a procedure mimics the pre-heating protocol performed each day during startup of the receiver. Additional coupons of each alloy were placed on fixtures that remained in the molten salt, so that isothermal samples could be compared with the thermally-cycled coupons.

Specimens of each alloy were removed from the molten salt mixtures at intervals of nominally 120, 240, 480, 800, 1600, 2400, and 4000 hours for examination. The principal measure of corrosion was descaled weight loss. The values reported in the following section were obtained from single coupons in all cases, as space limitations precluded replicated measurements. The coupons were descaled using a standardized procedure of boiling in alkaline permanganate solution followed by boiling in acidic citrate/EDTA solution.[14] These solutions removed all corrosion products with negligible attack of the underlying metal. The gravimetric data were converted to the equivalent amount of metal thickness loss based on the density of these stainless steels (7.96 gm/cm^3). At the end of the test, companion coupons, which were not descaled, were cross-sectioned and prepared for metallographic examination. Optical and scanning electron microscopy, electron microprobe analysis, and X-ray diffraction were used to characterize the structure and composition of the adherent corrosion products. Electron microprobe analysis was performed by a JOEL Superprobe Model 733 using standardless wavelength dispersive spectroscopy.

Figure 1. Crucible furnaces and mechanical cycling frame used to evaluate corrosion in molten nitrate salt during thermal cycling. The fixtures for the stainless steel coupons are visible at the top of the crucibles.

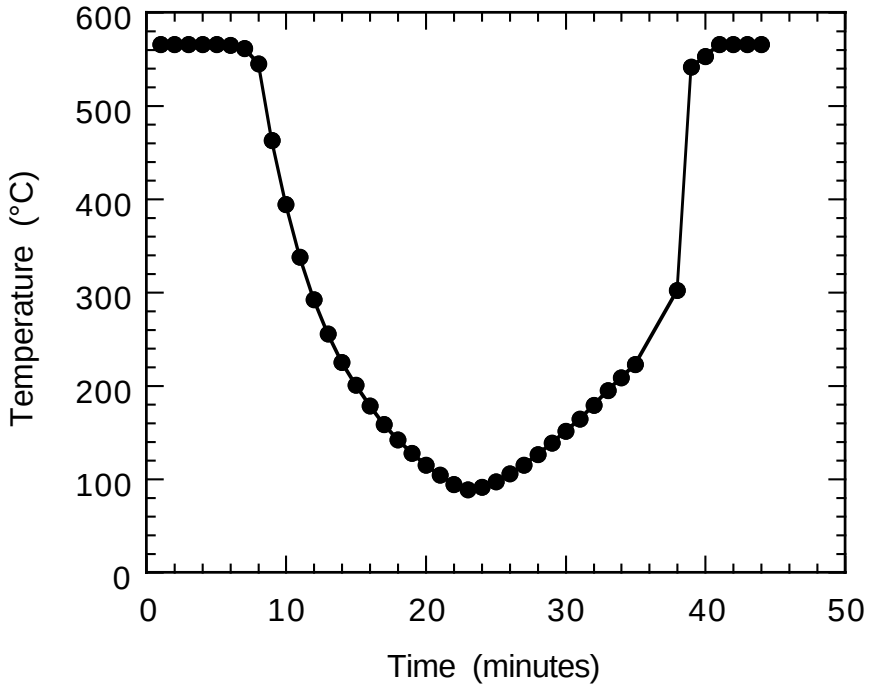

Figure 2. Temperature profile experienced by molten salt corrosion coupons during thermal cycling. The temperature was essentially constant at 560¡C during the remaining 7.5 hours (not shown) of the 8-hour period.

III. Results

Metal losses

The effect of thermal cycling on the corrosion rates of these stainless steels was determined by comparing descaled metal losses during thermal cycling and isothermal exposure to the molten salt. Comparisons of corrosion behavior among the alloys can be visualized most easily by plotting descaled metal losses as a function of time. The effect of dissolved chloride in the molten salt mixtures on corrosion can also be visualized by plotting descaled metal losses versus time. The metal loss plots shown below use the square root of time as the abscissa in order to facilitate the analysis of corrosion rate equations that is discussed later. The descaled metal loss measurements for the three types of stainless steels are summarized in Table A-1 (thermally-cycled tests) and Table A-2 (isothermal tests) in the Appendix. The tables summarize the measurements corresponding to the four salt mixtures at each sampling time.

316 SS The results concerning 316 SS are of primary interest as this alloy was used to construct the Solar Two receiver. The descaled metal losses of 316 SS during thermal cycling are shown in the upper graph in Figure 3 (see also Table A-1 in the Appendix). The lines shown in Fig. 3 (and Figures 4 and 5 which follow) represent data fitting to kinetic equations that are discussed in the next section. After 4084 hours and 510 thermal cycles, the descaled metal losses ranged from about 5 microns in molten salt mixtures M-1 and M-2, which had the lowest levels of dissolved chloride, to about 11 microns in the mixture doped with the highest level of NaCl (M-4). In relation to the service conditions expected in an SCR, the extent of corrosion measured here is quite moderate as 4000 hours and 500 thermal cycles exceed the usage that would likely be achieved during one year of on-sun operation. The isothermal metal loss data for 316 SS are shown in the lower plot in Figure 3 (see also Table A-2, Appendix). Fewer sampling intervals were used during the isothermal tests, although the duration of these tests was somewhat longer than the thermally-cycled test of 316 SS. After 4584 hours of isothermal immersion, the metal losses of 316 SS ranged from 4 to 5 microns in mixtures M-1 and M-2 to about 8 microns in the mixture doped with NaCl (M-4). In general, isothermal samples experienced somewhat less corrosion than thermally-cycled samples after comparable exposure time.

The effect of dissolved chloride on corrosion of 316 SS by molten nitrate salts is shown quite clearly by the metal loss plots in Figure 3. The chloride content of the molten salts had a significant effect on the corrosion behavior of 316 SS during thermal cycling. More dissolved chloride increased the corrosion rate and the effect was accentuated as exposure time increased. Isothermal corrosion was less sensitive to chloride impurities than thermal cycling, although here too, corrosion rates generally increased as the concentration of dissolved chloride in the molten salts increased. The mechanisms by which chloride ion contamination can degrade the oxidation resistance of alloys at elevated temperature have been reviewed by Hancock.[11] The most likely cause of increased corrosion in the molten nitrate salt environment is that chloride increases the porosity of the surface oxide layer. This aspect of corrosion behavior is discussed further in a subsequent section of the report concerning analysis of the corrosion products.

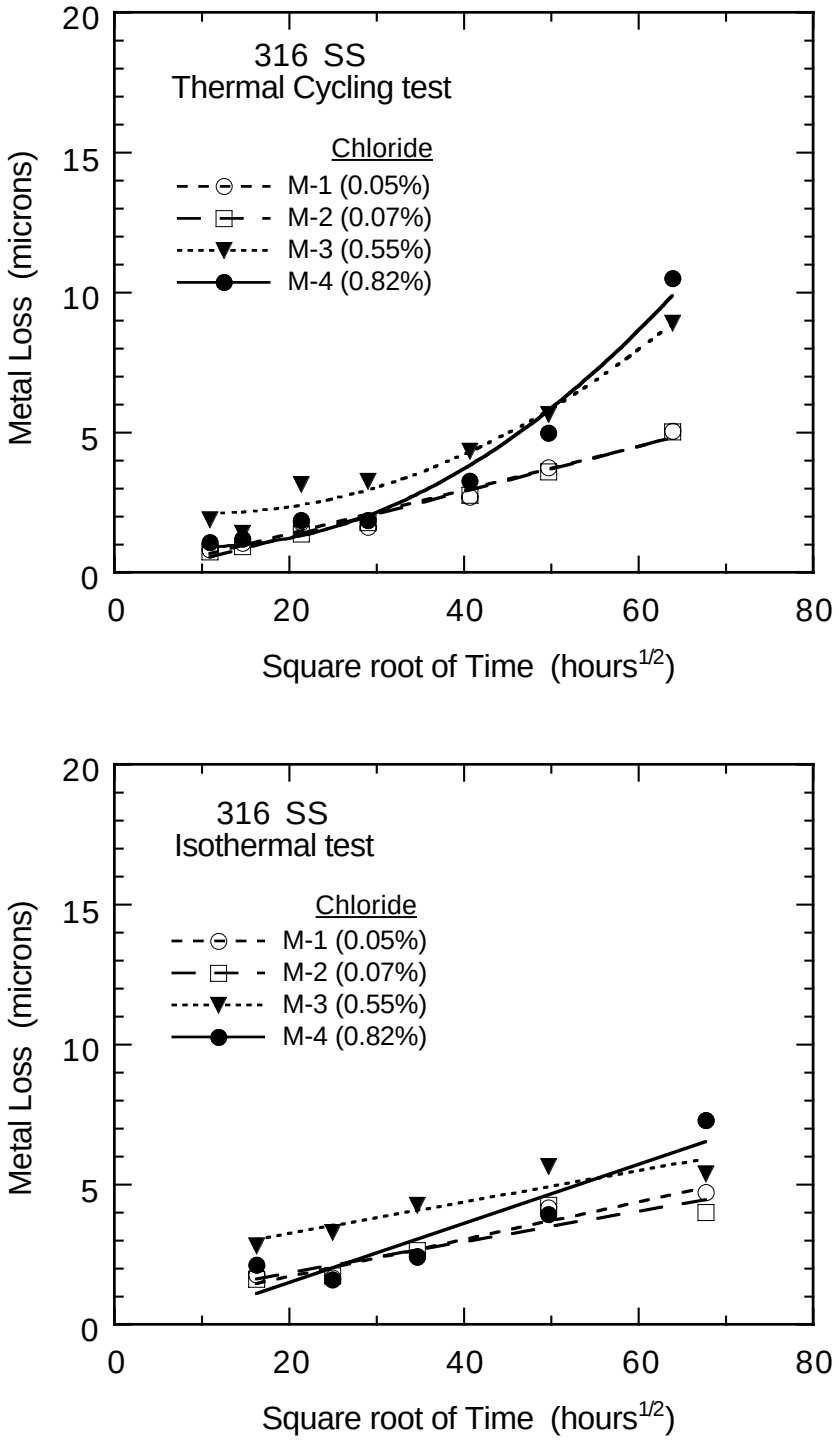

Figure 3. Descaled metal losses of Type 316 SS during corrosion in molten nitrate salt mixtures at 565°C, plotted using parabolic coordinates for the abscissa. Data for four levels of dissolved chloride are shown for thermal cycling (upper) and isothermal corrosion (lower).

316L SS Descaled metal loss measurements from thermal cycling tests of 316L SS are presented in the upper graph in Figure 4. The metal losses for 316L SS during thermal cycling were less than those of the other two stainless steels. After 4084 hours and 510 thermal cycles, the metal losses of 316L SS were slightly less than 6 microns in all of the salt mixtures. The corrosion data show little dependence on the dissolved chloride content of the molten salt mixtures as is evident from the tight grouping of the four lines shown in Fig. 3. The corresponding isothermal corrosion data for 316L SS are shown in the lower plot in Figure 4. After 4584 hours of immersion, the metal losses were slightly less than 5 microns in all of the salt mixtures. Such metal losses are only marginally lower than those of thermally-cycled samples after comparable exposure time.

Although 316L SS displayed slightly better corrosion resistance in the molten salt than 316 SS, this similarity is a marked contrast to corrosion of these two grades of stainless steel that is often observed in aqueous media. These stainless steels were tested at 565°C, a temperature at which the chromium in these alloys precipitates at grain boundaries, as chromium carbides, in a much shorter time than the duration of these tests.[15] Such precipitation aggravates intergranular corrosion of stainless steels in aqueous environments due to the depletion of chromium near grain boundaries, a phenomenon known as sensitization.[15] Because of sensitization, low-carbon versions of stainless steels are often specified to minimize intergranular attack, e.g., for welded structures in which the thermal conditions that produce sensitization are unavoidable. If carbide precipitation degraded the oxidation resistance of stainless steels by molten nitrate salts, we would expect to see some indication by comparing 316 SS and 316L SS, as 316L SS contains much less carbon than the heat of 316 SS used in these tests (see Table I). This is generally not the case, however, as the differences in corrosion losses of 316 SS and 316L SS in the molten nitrate salt environment are rather small as shown in Figures 3 and 4 (and Table A-1, Appendix), although Type 316L SS corrodes somewhat more slowly than 316 SS in the high-chloride molten salts. Furthermore, no intergranular corrosion of 316 SS occurred in the molten salt, as shown in the metallographic results presented later.

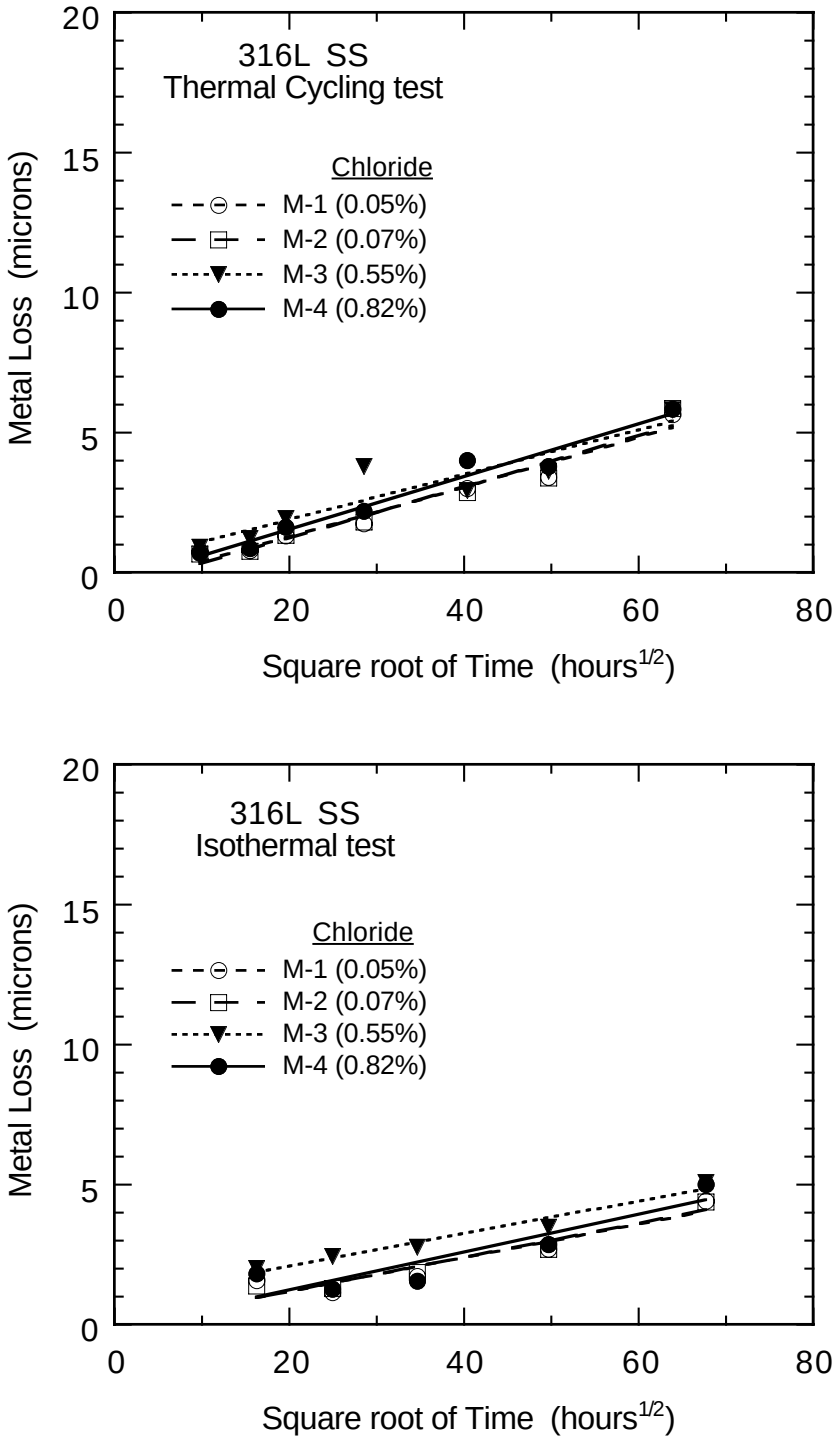

Figure 4. Descaled metal losses of Type 316L SS during corrosion in molten nitrate salt mixtures at 565°C, plotted using parabolic coordinates for the abscissa. Data for four levels of dissolved chloride are shown for thermal cycling (upper) and isothermal corrosion (lower).

304 SS Descaled metal loss measurements for the thermally-cycled 304 SS specimens are shown in the upper graph in Figure 5. The losses for this alloy were larger, by a factor of two or more in some cases, than those of either grade of 316 SS and were also the most sensitive to the chloride concentrations of the molten salt mixtures. After 4432 hours and 554 thermal cycles, the metal losses ranged from about 8 microns in the low-chloride salt mixtures M-1 and M-2 to 16 microns in the mixture doped with NaCl (M-4). The corresponding isothermal corrosion data for 304 SS are shown in the lower plot in Figure 5. After 4584 hours of immersion, the metal losses of 304 SS ranged from about 6 microns in mixtures M-1 and M-2 to 16 microns in the mixture doped with NaCl (M-4). Metal losses of isothermal coupons were slightly less than those of the corresponding thermally-cycled samples of 304 SS after comparable exposure time.

The metal losses of 304 SS are plotted in Figure 5 using the same format as Figs. 3 and 4. The chloride content of the molten salts had a significant effect on the corrosion behavior of this alloy during either thermal cycling or isothermal exposure. As described above for 316 SS, more dissolved chloride increased the corrosion rate of 304 SS and the effect was particularly evident as exposure time increased. Isothermal corrosion was less sensitive to chloride impurities than thermal cycling, although isothermal corrosion rates generally increased as the concentration of dissolved chloride in the molten salts increased. The most corrosion of any of the test conditions occurred for 304 SS in the high-chloride salt (M-4, 0.82%). In addition, the salt mixture containing the highest chloride level caused a change in the time dependence of the corrosion process. This aspect of corrosion behavior is discussed later in the report.

Generally, the corrosion data obtained during the current isothermal test at 565¡C agree well with data obtained in a previous isothermal test conducted at 570¡C.[3] In the earlier tests, the metal losses of 316 SS were 4-6 microns and 304 SS were 6-8 microns after 4000 hours, depending on the chloride content of the molten salt. The moderately better corrosion resistance of 316 SS compared to 304 SS observed here is consistent with the results of the earlier isothermal tests. Visual inspection of coupons of the three stainless steels after more than 4000 hours of thermal cycling did not show much evidence that the oxide spalled to expose the base metal. This contrasts with our observations during previous isothermal corrosion tests.[3] The coupons in the earlier tests were used in the as-received condition and had various surface finishes that appeared to result from rolling of the sheets. In the tests reported here, we used a standard procedure of grinding the coupons with 120 grit sandpaper. The differences in oxide adherence between these two sets of experiments is likely to be related to the different surface preparation methods.

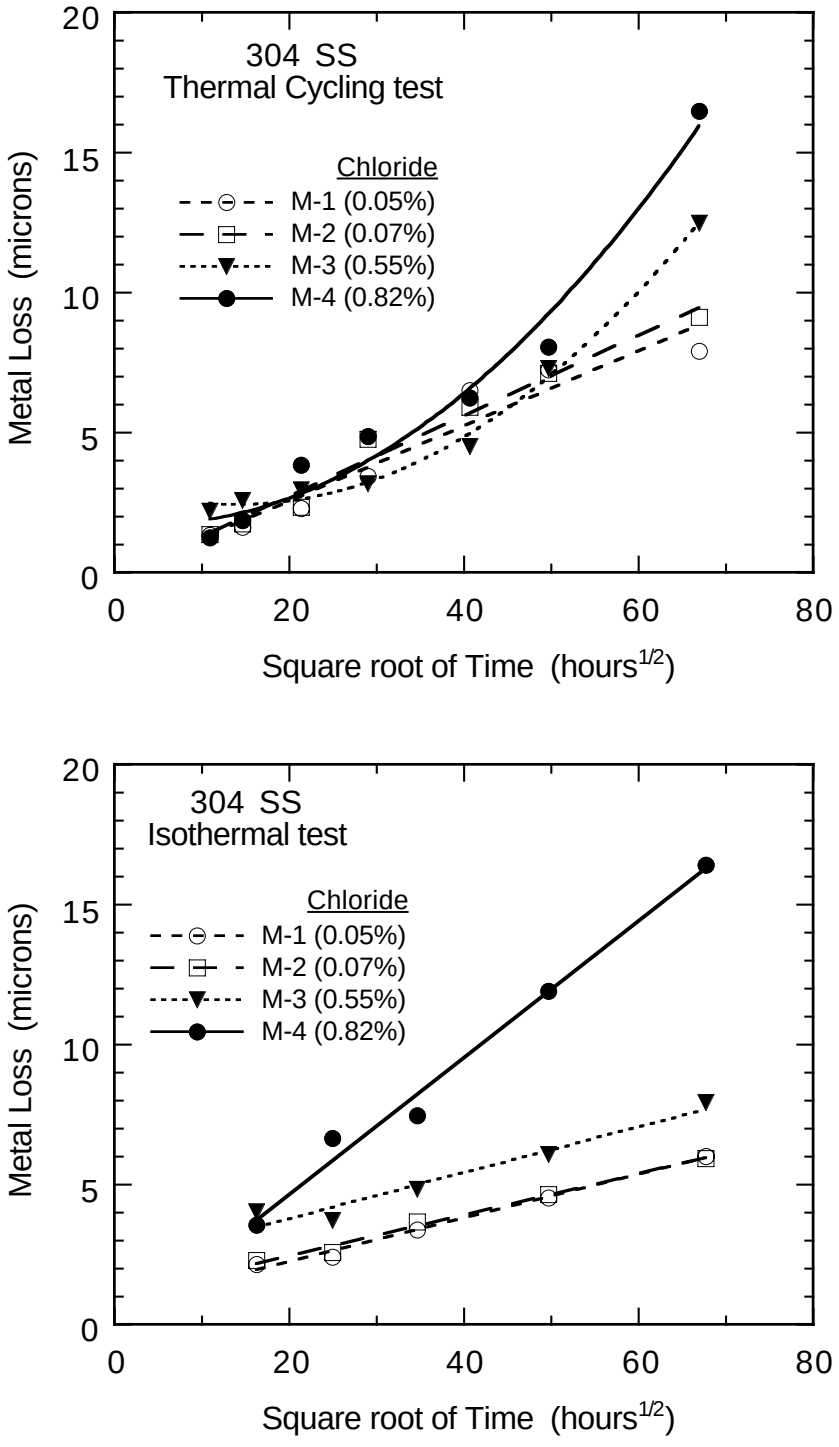

Figure 5. Descaled metal losses of Type 304 SS during corrosion in molten nitrate salt mixtures at 565¡C, plotted using parabolic coordinates for the abscissa. Data for four levels of dissolved chloride are shown for thermal cycling (upper) and isothermal corrosion (lower).

Corrosion kinetics

The time dependence of metal loss data can often be used to infer a corrosion mechanism. For example, metal losses that increase in proportion to the square root of time imply that the surface scales grow by a self-limiting process that is controlled by diffusion of one of the chemical species that constitute the scale. Such a corrosion process is typically referred to as following "parabolic" kinetics. Another common correlation is metal loss that increases linearly with time. Linear kinetics can arise in several ways. For example, the corrosion product layer may be porous and therefore not present an effective diffusion barrier to the corrosive agent in the environment. Similarly, an non-protective layer may be formed by a sequence of growth of a non-porous oxide, spalling or cracking of that oxide, and a resumption of growth that is repeated many times during the experimental time interval. Such repetition would yield, in aggregate, a linear process.

The metal loss data were correlated using the two most common equations of corrosion kinetics described above to provide a basis for extrapolating the data to longer service periods, as well as to better understand the type of corrosion behavior occurring in the molten salt environment. We used the approach suggested by Pieraggi and plotted the metal losses vs. the square root of time (a parabolic plot) rather than alternative methods, such as log-log or squared metal loss vs. time plots.[16] This graphical approach clearly differentiates between parabolic kinetics and linear kinetics. Linear kinetics are identified on such a parabolic plot as data that increasingly diverge upward from a straight line as time increases. The data for 316 SS during thermal cycling (see Figure 3, upper) illustrate how linear kinetics contrast with parabolic kinetics. Metal losses observed in low-chloride mixtures M-1 and M-2 are represented by straight lines in these parabolic coordinates (note that the data for M-1 and M-2 virtually overlay one another). Parabolic kinetics thus describe corrosion in these salt mixtures. In contrast, the data for high-chloride mixtures M-3 and M-4 display pronounced upward curvature indicative of linear kinetics.

Regression analysis of the metal loss data in Figures 3, 4 and 5 was performed using the software application Kaleidagraph (Abelbeck Software, Reading, PA). The lines shown in these figures represent data fitting to these kinetic equations. Parabolic rate constants, k_p, were determined for each combination of stainless steel and molten salt mixture using rate equation (1).

(1) $\text{metal loss} = k_p \_\text{time})^{1/2} + a_p$

The regression program also provided correlation coefficients that indicate the goodness-of-fit. Data that were not correlated well by a parabolic equation were fitted using a linear rate equation (2) below, where k_l is the linear corrosion rate constant.

(2) $\text{metal loss} = k_l\,(\text{time}) + a_l$

The analysis of corrosion rate equations given here provides estimates of the rate constants and some insight regarding trends in kinetics. However, the variance of the metal loss data could not be calculated as only single values were measured at each time due to the limited number of coupons that could be mounted on the fixtures. Thus, statistical confidence limits could not be obtained for the rate constants. Regardless of these constraints, several trends appear

consistently in our data. The corrosion rate constants obtained from the regression analysis are summarized in Table III. In general, the values of k_p indicate that the rate constants were consistently greater for thermal cycling compared to isothermal corrosion, and as the dissolved chloride concentration of the molten salt increases. The rate constants were also higher when these alloys were immersed in the high-chloride salt mixture (M-4) compared to the rate constants in the low-chloride salt, M-1, that was used as the basis for formulating mixture M-4. The values in Table III also indicate that 304 SS is less corrosion resistant than either grade of 316 SS at all of the testing conditions.

Linear rate constants are indicated by the shaded boxes in Table III. One may observe from the table that the only environmental conditions that give rise to linear oxidation kinetics are those that subject the surface oxide layers to both thermal cycling and relatively high concentrations of dissolved chloride ion, e.g., 0.55 wt.%. and 0.82 wt.%. Both of these conditions tend to diminish the ability of oxide films to form protective barriers, as noted in the Introduction.

Table III. Rate constants for metal loss of stainless steels during either thermal cycling or isothermal corrosion in molten nitrate salts. The values shown are parabolic rate constants except for the shaded boxes, which denote linear rate constants. The concentration (wt.%) of chloride ion impurities in each molten salt mixture is indicated by the parenthetic values.

Stainless Steel	Test Conditions	Rate constants *			
		M-1 (0.05%)	M-2 (0.07%)	M-3 (0.55%)	M-4 (0.82%)
316 SS	Cyclic	1.3	1.4	0.49†	0.64
	Isothermal	1.1	0.93	0.93	1.8
316L SS	Cyclic	1.5	1.5	1.4	1.6
	Isothermal	1.0	1.0	0.98	1.1
304 SS	Cyclic	2.3	2.4	0.65	0.90
	Isothermal	1.3	1.2	1.4	4.1

* The units of parabolic rate constants are 10^{-7} cm/sec$^{1/2}$.

† The units of linear rate constants are 10^{-10} cm/sec.

Microanalysis of corrosion products

We examined the microstructure of the surface oxide layers formed during corrosion in the molten salt to determine what differences in their structure or composition were associated with the type of oxidation rate equations observed in the various salt mixtures. Optical microscopy of a cross-sectioned coupon of each type of stainless steel established that the oxide scales were generally adherent, regardless of temperature cycling or the impurities in the molten salt mixtures. Similarly, the average thickness of the oxide layers observed microscopically was consistent with stoichiometric calculations based on the descaled metal losses. Because the oxide consists primarily of M_3O_4-type spinels, the scale thickness, in microns, is given approximately by the descaled metal loss, in microns, multiplied by 2.1. The microscopic observations were consistent with this relationship. Regardless that scattered locations were found at which the scale had detached, metallographic analysis of the coupons revealed significant information concerning the structure of protective and non-protective oxide layers formed in the molten salt.

Scanning electron microscopy was used to characterize the morphology of the surface scales and electron microprobe analysis (EMP) was used to determine the elemental composition of the corrosion products on several thermally-cycled specimens that had been exposed for the entire test period. In addition to analysis of cross-sectioned coupons, X-ray diffraction was used to identify the oxide compounds on a few coupons. As the number of corroded coupons generated during this study was quite large, only a limited number could be analyzed in detail. EMP analysis was used to inspect the 316 SS coupon that corresponded to the slowest corrosion rate (from mixture M-1), and coupons of 304 SS that corresponded to the slowest (parabolic) corrosion rate for that alloy (from M-1) and the most rapid, and linear, corrosion rate (from M-4). We particularly sought to determine if structural differences existed between the oxide layers that formed on samples exhibiting parabolic kinetics as opposed to linear oxide growth.

The microstructure of the oxide scale formed on 316 SS after 4084 hours of thermal cycling in the low-chloride salt mixture M-1 is shown in Figure 6 (upper). The surface scale shown in this photomicrograph is approximately 6 microns thick and is typical of that appearing around the entire periphery of this cross-sectioned coupon. This micrograph is a backscattered electron (BSE) image and the contrast in the corrosion layers reflects the sensitivity of BSE to the atomic weight of the constituents. Regions having higher average atomic weight appear relatively brighter than localities having lower atomic weight. The slight differences in contrast in the image suggest that the oxide scale is comprised of three layers, which are indicated by the brackets at the upper right side. The elemental composition of these oxide bands was determined by EMP and these data are presented graphically by the bar chart in Figure 6. The bar chart does not show the iron content, which formed the balance of the elemental composition except for a few percent of molybdenum. The numbered entries in the ordinate labels correspond to the numbered locations shown on the micrograph and represent analyzed areas about 1-2 microns in diameter. The data shown in the chart are averages of the spot locations corresponding to each region of the corrosion products and underlying alloy. The averages were used for convenience as the variations in the corresponding spots were not significant.

The elemental concentration data for 316 SS clearly reveal that the outer layer (points 7 and 8) consists of iron, sodium, and oxygen. This layer was in direct contact with the molten salt. X-ray diffraction analysis indicated that this phase is sodium ferrite, $NaFeO_2$. The middle layer (points 6 and 9) consists primarily of iron and oxygen, with a minor amount of chromium and much less sodium than the outer layer. X-ray diffraction identified this phase as magnetite, Fe_3O_4. The inner layer, corresponding to points 4, 5, and 10 in Fig. 6, is an iron oxide that contains a significant amount of chromium, as well as some nickel. This layer also has the spinel structure of magnetite. The inner layer contains about the same proportion of molybdenum as the alloy, while this element is absent from the top and middle layers. The EMP data also indicate that the sub-layer of the alloy immediately beneath the oxide layers is depleted in chromium and enriched in nickel (see analysis of spots 3 and 11) as compared to the unaffected alloy (e.g., see analysis of spots 1, 2, 12 and 13).

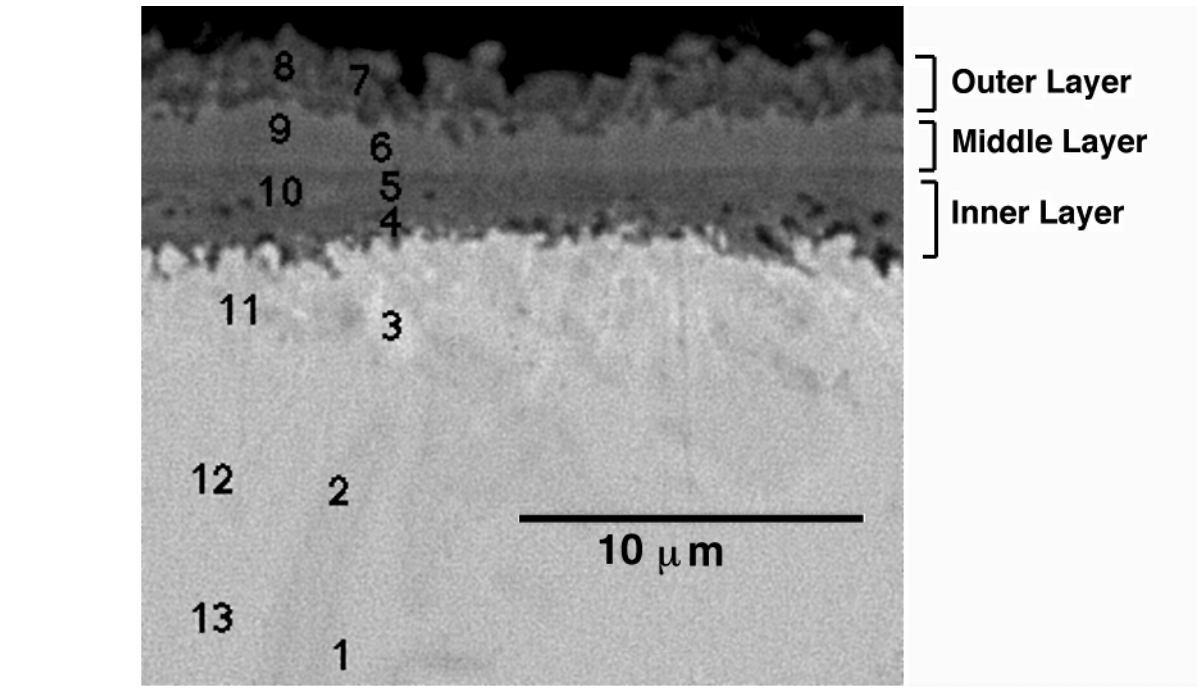

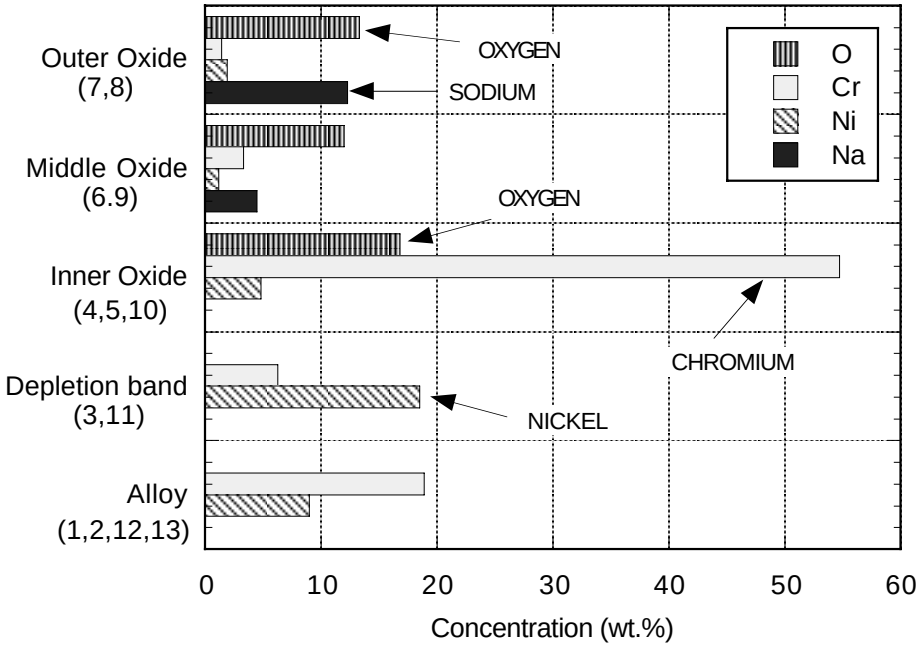

Figure 6. Back-scattered electron micrograph of corrosion product layers on 316 SS after thermal cycling to 565¡C (max.) for 4084 hours in a molten nitrate salt mixture (M-1) containing 0.05 % chloride. The elemental analyses corresponding to the numbered locations on the micrograph are shown by the bar chart. The balance of the elemental composition, iron, is not shown on the chart.

Figure 7 shows a BSE image of the oxide scale on a 304 SS coupon that was thermally-cycled in the low-chloride salt mixture M-1 for 4084 hours. The metal loss kinetics for these conditions followed a parabolic equation. The oxide layer formed on 304 SS was somewhat thicker (approximately 10 microns) than that on 316 SS exposed to the same environment, in agreement with the descaled metal losses shown in Figs. 3 and 5. The general structure of the oxide layers on 304 SS was similar to that on 316 SS (as shown in Fig. 6) in that three layers can be distinguished. The bar chart in Fig. 7 shows the elemental distribution of the principal alloying elements of 304 SS, as well as oxygen and sodium. The elemental concentration data indicate that the outer layer (points 8 and 9) consists of iron, sodium, and oxygen. X-ray diffraction analysis identified that this phase as sodium ferrite, $NaFeO_2$. The middle layer (points 7 and 10, 6 and 11, and 5) consists primarily of iron and oxygen, and a minor amount of chromium. The sodium content in the middle layer is small at the interface with the outer layer and diminishes to zero as depth increases. X-ray diffraction identified this phase as magnetite, Fe_3O_4. The inner layer, corresponding to points 4 and 12 in Fig. 7, is an iron-chromium spinel oxide that contains a significant amount of chromium, as much as 60 wt.%. The EMP data also indicate that the sub-layer of the alloy immediately beneath the oxide layers is depleted in chromium and enriched in nickel (spots 3 and 13) as compared to the unaffected alloy (spots 1, 2, 14 and 15).

Both 316 SS and 304 SS followed parabolic corrosion kinetics in the low-chloride molten salt, which implies that at least one of the oxide layers shown in Figures 6 and 7 constituted a diffusion barrier to metal or oxygen. In both cases, a spinel layer that contained an appreciable amount of chromium was formed adjacent to the alloy. This suggests that this particular layer constitutes the protective barrier for these alloys. This point is discussed further later in the report. The general morphology of the corrosion products shown in Figures 6 and 7 is also representative of the corrosion products formed on 316L SS, although the thickness of the layers on the low-carbon steel was somewhat less.

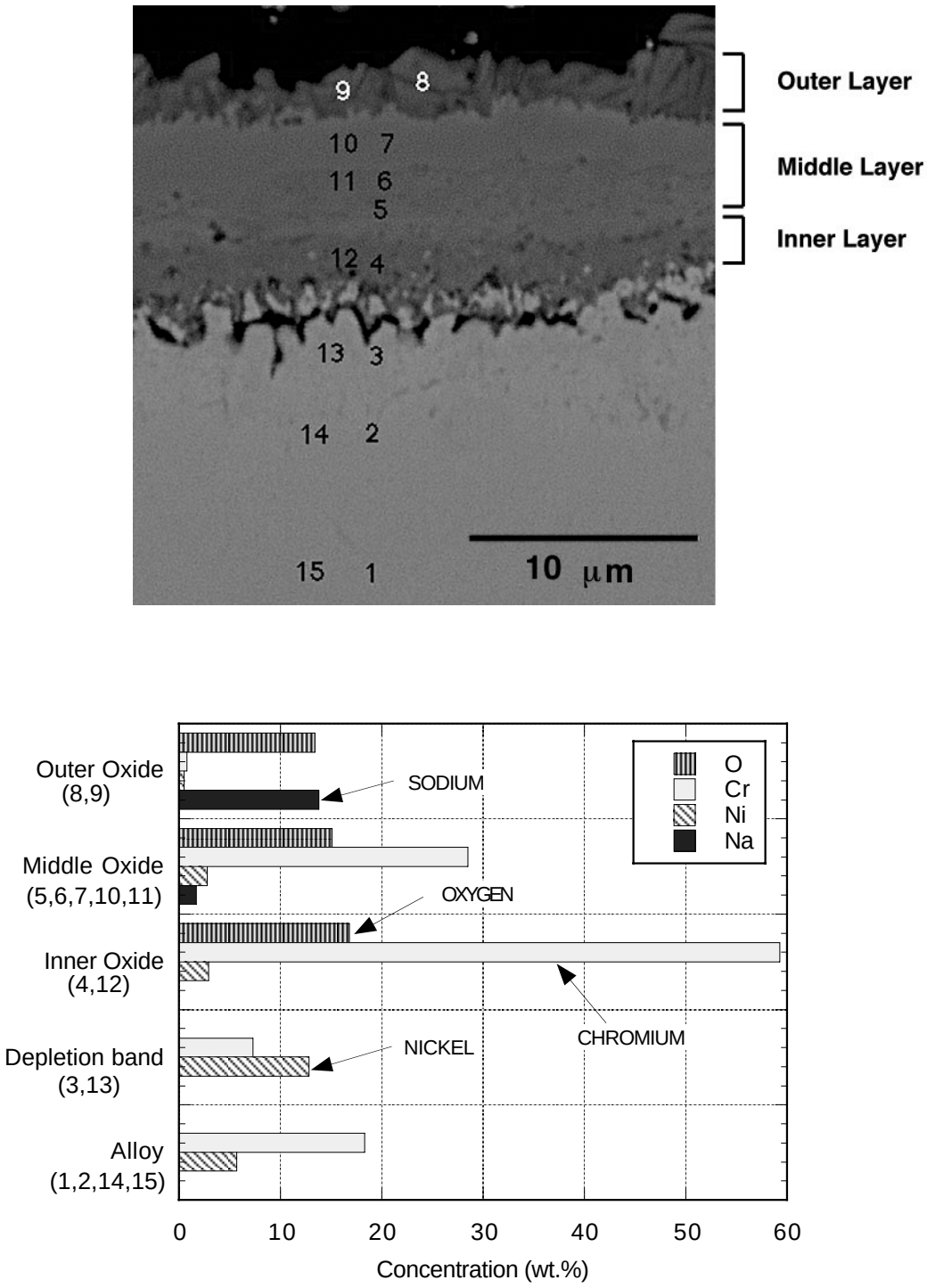

Figure 7. Back-scattered electron micrograph of corrosion product layers on 304 SS after thermal cycling to 565¡C (max.) for 4084 hours in a molten nitrate salt mixture (M-1) containing 0.05 % chloride. The elemental analyses corresponding to the numbered locations on the micrograph are shown by the bar chart. The balance of the elemental composition, iron, is not shown on the chart.

The occurrence of linear corrosion kinetics is of considerable practical interest in estimating the lifetime of SCR tubes. Metal consumption under such circumstances may become quite large, compared to parabolic kinetics, during the 20 to 30 years of service expected from this assembly. For this reason, the coupon that displayed the most rapid linear corrosion rate was examined for comparison with the samples discussed above. A representative example of the multilayered oxide structure formed on 304 SS after 4084 hours of thermal cycling in the high-chloride nitrate salt mixture, M-4, is shown by the BSE micrograph in Figure 8. EMP analysis of a coupon of 316 SS that had been thermally-cycled in the high-chloride salt mixture, M-4, for 4084 hours, and which also experienced linear corrosion kinetics yielded similar results regarding the structure and composition of the oxide layers, as described below for 304 SS.

Several features are notable in the structure of the oxide layers associated with linear kinetics. One readily apparent difference is that the corrosion products shown in Fig. 8 are much thicker (about double) than those in the previous two figures. Other significant differences concern the composition of the oxide scale on the coupon exposed to the high-chloride molten salt. As indicated by the bar chart that accompanies Fig. 8, EMP data revealed that the oxide layer adjacent to the alloy has far less chromium (~11%) as compared to the two samples (~60%) discussed above. In addition, sodium is present in the inner oxide scale, rather than absent as in either of the two samples discussed previously. Sodium can be detected throughout most of the oxide layer, although the concentration decreases as the distance from the salt-contacting outer surface increases. The proportions of chromium and iron in the inner oxide layer of the coupon shown in Fig. 8 are reversed compared to the samples displaying parabolic rate equations. The analysis of spots 5 and 6 indicated only 10-20% Cr versus about 50% in the other coupons. Typically, less chromium implies a less protective oxide layer and more rapid corrosion rates.[12, p. 365ff] The morphology of the inner oxide band is much less uniform than those shown in Figures 6 and 7. Sub-micron sized islands that appear to be unoxidized metal (e.g., the white spots to the left of spot 6 in Fig. 8) can be observed. Some porosity is also evident, but voids may result from pull-out during metallographic preparation rather than defects growing in the oxide scale.

The EMP data revealed that the corrosion products contained no chlorine in any form. When chloride does not participate in chemical reactions with alloying elements, the primary mechanism that aggravates corrosion results from the adsorption of chloride on surfaces, such as the oxide-metal interface or oxide grain boundaries.[11] Such adsorption disrupts the coherent growth of the surface oxide layer. At very high concentrations, chloride adsorption can degrade adhesion of the scale sufficiently to cause oxide layers to spall. In the present tests in which the oxide scales remained adherent, increasing amounts of adsorbed chloride may enhance the porosity of the NiO layer. As the porosity of the scale increases, the alloy-oxide interface becomes more accessible to the molten salt, thereby promoting the removal of soluble alloying elements and faster corrosion.

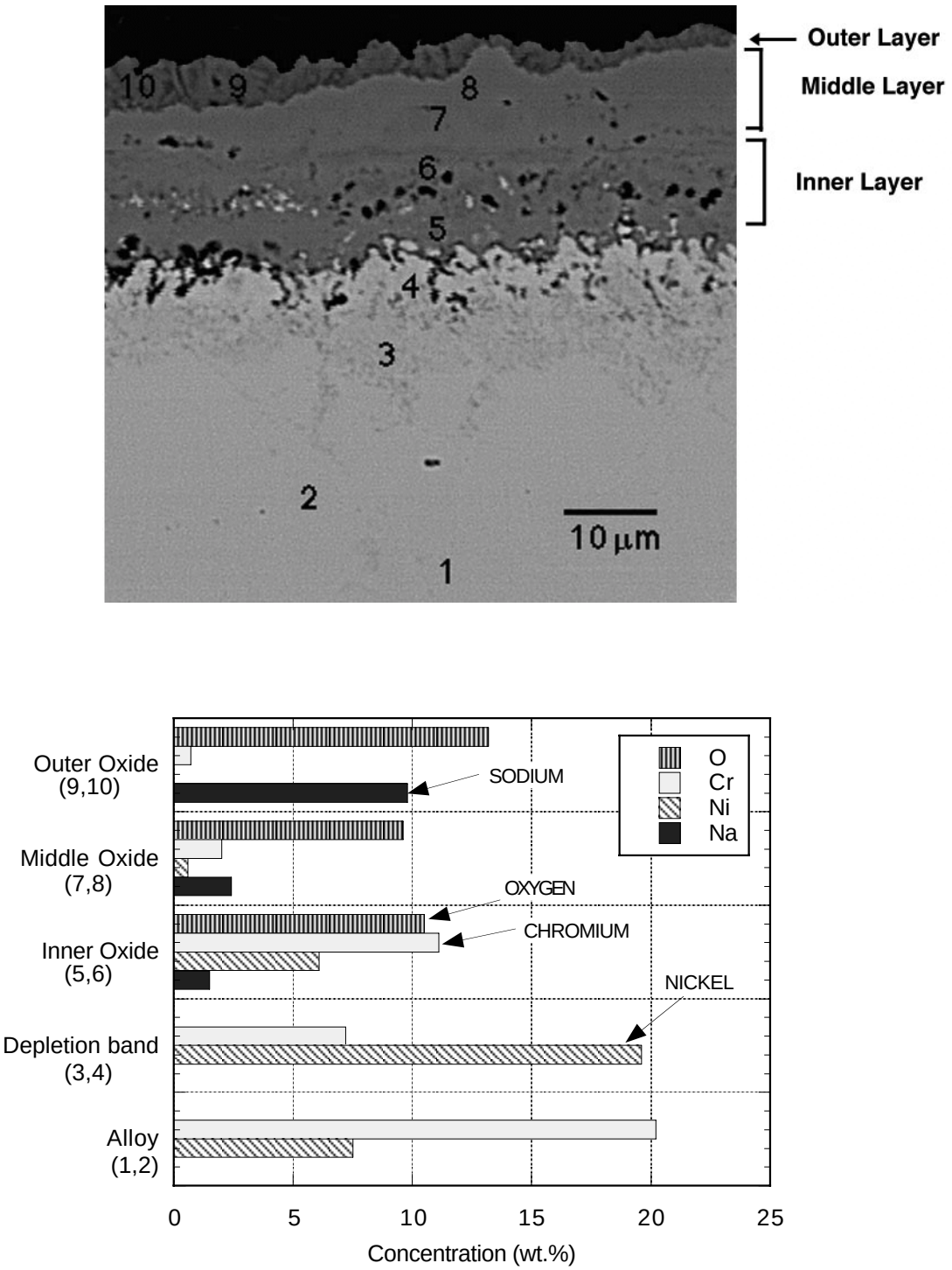

Figure 8. Back-scattered electron micrograph of oxide scale layers on 304 SS after thermal cycling at 565°C for 4084 hours in a molten nitrate salt mixture (M-4) containing 0.82 % chloride. The elemental analyses corresponding to the numbered locations on the micrograph are shown by the bar chart. The balance of the elemental composition, iron, is not shown on the chart.

The preceding descriptions of the microstructure of the oxide layers remnant on various samples demonstrates that one can distinguish between two very different modes of oxidation behavior of these alloys using EMP. EMP analysis revealed that the Cr content of the inner oxide layer of protective scales, which corrode according to parabolic kinetics, is much higher than that of the corresponding scale layer on samples that corrode according to linear kinetics. This elemental analysis provides an important tool for assessing corrosion performance in operating systems. The implication of this observation is that post-mortem EMP examination of metallurgical samples removed from an operating plant can indicate whether parabolic or linear kinetics have governed the oxidation behavior to that point in time. Given the extent of corrosion observed on such samples, the rate equation may be extrapolated to provide a reasonable estimate of the remaining operating lifetime of the component.

IV. Discussion

The corrosion behavior of stainless steels in other high-temperature, weakly-oxidizing environments, such as steam and carbon dioxide, have been widely reported in the literature for temperatures comparable to those intended for SCR systems. Of special interest here are the studies of oxidation by steam because the superheater in the steam generator of an SCR system operates at temperatures up to 565°C, the same as conventional electrical power systems.[3] A comprehensive review of metal loss data for stainless steels in steam environments has been published [13] and these data are plotted in Figure 9 along with comparable data for molten nitrate salt from this study. The parabolic rate constants for metal loss in steam vary from $3x10^{-7}$ $cm/sec^{1/2}$ to $5x10^{-6}$ $cm/sec^{1/2}$ at a temperature of 565°C, as shown in Figure 9. These rate constants pertain to formation of a duplex oxide layer consisting of a layer of magnetite over a layer of iron-chromium spinel where both layers are about equal in thickness. In the iron-chromium spinel portion of the duplex oxide, the proportions of the metals usually mimic that present in the alloy, thus the oxide is richer in iron than chromium.[17,18] The wide variation in rate constants in steam shown in Fig. 9 is due to many factors, including surface finish, variations in alloy composition, etc. The values of k_p for 316 SS in molten nitrate salt, given in Table III, are also plotted in Figure 9. The molten salt data derive from both isothermal and thermal-cycling exposure to molten salts containing various amounts of chloride impurities. By comparison, the parabolic rate constants in the molten salt environment are considerably lower. We hypothesize that this is because the chromium-containing oxide layer formed in molten salt is richer in chromium than the layers that appear to be formed in steam at the same temperature.[17,18] As shown by the electron microprobe analyses in Figures 6 and 7, the concentration of chromium in the oxide layers formed in the molten salt approached 50 wt.%, while the steam environment ordinarily results in only about 20 wt.% chromium in the spinel layer. Figure 9 also displays the rate constants that were observed in steam when circumstances gave rise to a chromium sesquioxide (Cr_2O_3) layer. These rate constants, represented by the solid line, are much lower than those corresponding to duplex oxidation. However, such low rate constants cannot occur in the molten salt environment because Cr_2O_3 would dissolve if it were formed on the surface.[19]

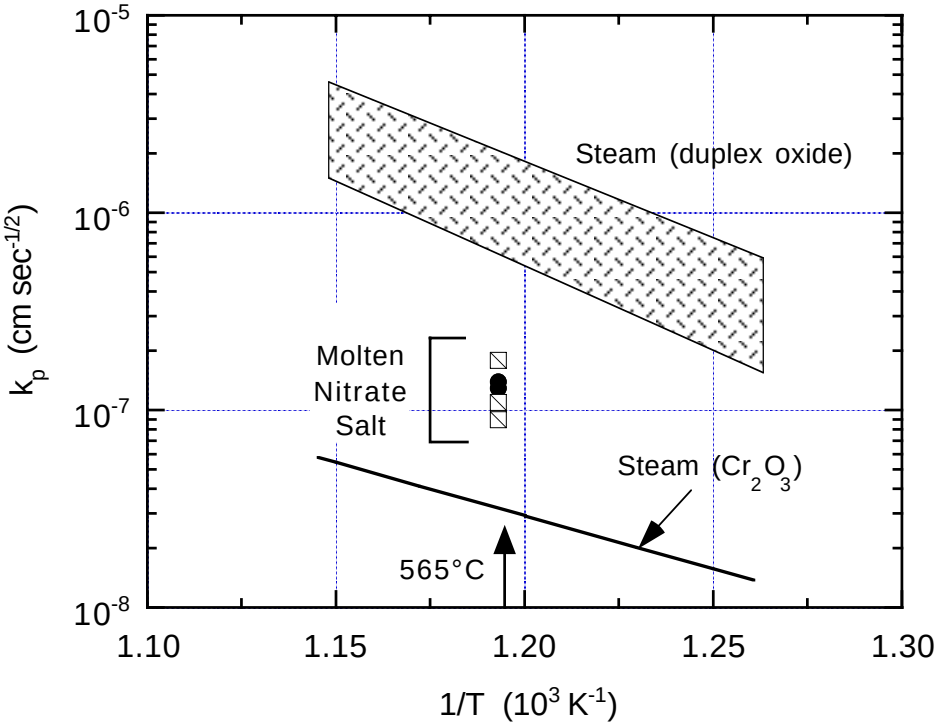

Figure 9. Parabolic rate constants for metal loss of 316 SS in molten nitrate salt compared to oxidation by steam. The data for steam are taken from Ref. 17. The molten nitrate salt data derive from testing, either isothermally or during thermal-cycling, at 565¡C in salt mixtures containing various amounts of chloride impurities.

V. Conclusions

Thermal cycling increased the corrosion rates of three stainless steels compared to isothermal immersion in the molten salt, but the increases were moderate. Type 316 SS experienced from 25% to 50% more corrosion during thermal cycling compared to isothermal exposure, depending on the chloride content of the molten salt. Type 316L SS demonstrated the least effect of thermal cycling, exhibiting no more than about a 25% increase in corrosion during the 4000-hour testing period. Type 304 SS corroded up to 50% more when thermally cycled, again, depending on the chloride content of the molten salt. The total metal losses experienced by these alloys ranged from about 5 microns to 16 microns after more than 4000 hours and 500 thermal cycles of exposure to the molten salt. Based on this data, we expect that receiver tubes constructed of 316 SS tubing should perform satisfactorily for a number of years.

Parabolic rate laws described corrosion kinetics reasonably well for most combinations of alloy, temperature conditions, and molten salt impurity concentrations that were tested. The parabolic rate constants for molten salt corrosion were lower than rate constants reported in the literature for high temperature steam oxidation of 316 SS. However, relatively high concentrations of dissolved chloride ions in the nitrate salt increased corrosion rates and tended to cause corrosion kinetics to follow linear rate equations under thermal cycling conditions. Elemental analysis of the corrosion products on the stainless steel coupons by electron microprobe revealed that the products consisted of several types of iron-based oxides, that contained chromium, as well as sodium from the molten salt. The oxides phases were organized in a multi-layered structure and the rate-controlling layer appears to be an iron-chromium spinel that forms adjacent to the alloy. In those instances in which parabolic kinetics occurred, the chromium content of this spinel layer was relatively large. Linear kinetics were observed when the spinel layer was relatively lean in chromium relative to the iron content. This correlation implies that microprobe analysis of stainless steel specimens removed from components in operating molten salt systems may be a useful diagnostic method to assess the state of health of those components.

VI. References

1. M. R. Prairie, J. E. Pacheco. G. J. Kolb and J. P. Sutherland, "Solar Central Receiver Technology: The Solar Two Project ", 1996 Annual A.I.Ch.E. Heat Transfer Conference, Houston, TX, Aug. 3-5, 1996.

2. P. DeLaQuil, B. Kelly and R. Lessley, "Solar One Conversion Project", *Solar Energy Mater*., 24, 151 (1991).

3. S. H. Goods, R. W. Bradshaw, M. R. Prairie and J. M. Chavez, "Corrosion of Stainless and Carbon Steels in Molten Mixtures of Industrial Nitrates", Sandia National Laboratories, SAND94-8211, March 1994.

4. R. W. Bradshaw, "Corrosion of 304SS by Molten $NaNO_3$-KNO_3 in a Thermal Convection Loop", Sandia National Laboratories, SAND80-8856, December 1980.

5. Martin-Marietta Corp., "Advanced Central Receiver Power System, Phase II, Vol. III. Molten Salt Materials Tests", Sandia National Laboratories, Contractor report SAND81-8192/3, Jan. 1984.

6. S. H. Goods, "Mechanical Properties of Alloy Steels in Molten Sodium-Potassium Nitrate Salts", in High Temperature Corrosion in Energy Systems, M. F. Rothman, Editor, The Metallurgical Society of A.I.M.E., 1985.

7. R. Mevrel, "Cyclic Oxidation of High-Temperature Alloys", *Mater. Sci. Tech.*, 3, 531 (1987).

8. M. Walter, M. Schultze and A. Rahmel, "Behavior of Oxide Scales on 12Cr-1Mo Steel during Thermal Cycling", *Oxid. Metals*, 39, 389 (1993).

9. J. J. Stephens, R. E. Semarge and R. W. Bradshaw, "Characterization of Oxide Scale Formed on Incoloy 800 Tubes in the Molten Salt Electric Experiment", in Microbeam Analysis-1986, A. D. Romig and W. F. Chambers, Editors., p. 337, Microbeam Analysis Society, 1986.

10. R. W. Bradshaw, 'Thermal-Convection Loop Study of Corrosion of Incoloy 800 in Molten $NaNO_3$-KNO_3', *Corrosion*, 43 (3), 173 (1987).

11. P. Hancock, "Vanadic and Chloride Attack of Superalloys", *Mater. Sci. Tech.*, 3, 536 (1987).

12. *High Temperature Corrosion*, P. Kofstad, Elsevier Science Publishing Co., New York, NY, 1988, p. 503ff.

13. D. A. Nissen and D. E. Meeker, "Nitrate/Nitrite Chemistry in $NaNO_3$-KNO_3 Melts", *Inorg. Chem.*, 22, 716 (1981).

14. N. A. C. E. Technical Practices Committee, “Procedures for Quantitative Removal of Oxide Scales Formed in High Temperature Water and Steam”, *Materials Performance*, 6, 69 (1967).

15. Corrosion of Stainless Steels, A. J. Sedricks, Wiley-Interscience, New York, NY, 1979, p. 120ff.

16. B. Pieraggi, “Calculation of Parabolic Reaction Rate Constants”, *Oxid. Metals*, 27, 177 (1987).

17. J. Armitt, D. R. Holmes, M. I. Manning, D. B. Meadowcroft and E. Metcalf, "The Spalling of Steam Grown Oxide from Superheater and Reheater Tube Steels”, Central Electricity Generating Board (U.K.), RD/L/R-1974, February 1978.

18. Behavior of Superheater Alloys in High Temperature, High Pressure Steam, G. E. Lien, Editor, A.S.M.E., New York, NY, 1968, p. 56ff.

19. D. H. Kerridge, “Chemistry of Molten Nitrates and Nitrites”, in MTP International Review of Science, C. C. Addison and D. B. Sowerby, Editors, Vol. 2, p. 29 (1972).

VII. APPENDIX

Table A-1. Descaled metal losses of 316 SS, 316L SS, and 304 SS during thermal-cycling at a maximum temperature of 565¡C in several molten nitrate salt mixtures. The concentration (wt.%) of chloride ion impurities in each molten salt mixture is indicated by the parenthetic values.

Time (hours)	Cycles (#)	Descaled metal loss (microns)			
316 SS		M-1 (0.05 Cl^-)	M-2 (0.07 Cl^-)	M-3 (0.55 Cl^-)	M-4 (0.82 Cl^-)
120	15	0.8	0.7	1.9	1.1
240	30	1.1	0.9	1.4	1.2
456	57	1.8	1.4	3.2	1.9
840	105	1.6	1.8	3.3	1.9
1656	207	2.7	2.8	4.4	3.3
2472	309	3.7	3.6	5.6	5.0
4084	510	5.0	5.0	8.9	10.5
316L SS		M-1 (0.05 Cl^-)	M-2 (0.07 Cl^-)	M-3 (0.55 Cl^-)	M-4 (0.82 Cl^-)
96	15	0.7	0.7	0.9	0.7
240	30	0.8	0.8	1.2	0.9
384	48	1.3	1.3	1.9	1.6
816	102	1.8	1.8	3.8	2.2
1632	204	3.0	2.9	2.9	4.0
2472	309	3.4	3.4	3.6	3.8
4084	510	5.7	5.9	5.8	5.8
304 SS		M-1 (0.05 Cl^-)	M-2 (0.07 Cl^-)	M-3 (0.55 Cl^-)	M-4 (0.82 Cl^-)
120	15	1.3	1.4	2.2	1.2
216	27	1.6	1.8	2.6	1.9
456	57	2.3	2.3	3.0	3.8
840	105	3.4	4.8	3.2	4.9
1656	207	6.5	5.9	4.5	6.3
2472	309	7.2	7.1	7.3	8.1
4432	554	7.9	9.1	12.5	16.5

Table A-2. Descaled metal losses of 316 SS, 316L SS, and 304 SS during isothermal corrosion at 565¡C in several molten nitrate salt mixtures. The concentration (wt.%) of chloride ion impurities in each molten salt mixture is indicated by the parenthetic values.

Time (hours)	Descaled metal loss (microns)			
316 SS	M-1 (0.05 Cl^-)	M-2 (0.07 Cl^-)	M-3 (0.55 Cl^-)	M-4 (0.82 Cl^-)
264	1.8	1.6	2.8	2.1
624	1.7	1.8	3.3	1.6
1200	2.4	2.6	4.3	2.4
2472	4.2	4.3	5.6	3.9
4584	4.7	4.0	5.4	7.3
316L SS	M-1 (0.05 Cl^-)	M-2 (0.07 Cl^-)	M-3 (0.55 Cl^-)	M-4 (0.82 Cl^-)
264	1.6	1.4	2.0	1.8
624	1.2	1.3	2.4	1.3
1200	1.7	1.9	2.8	1.6
2472	2.7	2.7	3.5	2.9
4584	4.4	4.4	5.1	5.0
304 SS	M-1 (0.05 Cl^-)	M-2 (0.07 Cl^-)	M-3 (0.55 Cl^-)	M-4 (0.82 Cl^-)
264	2.1	2.3	4.0	3.6
624	2.4	2.6	3.7	6.7
1200	3.4	3.7	4.8	7.5
2472	4.5	4.7	6.1	11.9
4584	6.0	5.9	7.9	16.4

VIII. DISTRIBUTION

1 Advanced Thermal Systems, Inc.
Attn: Mr. Robert Thomas
5031 W. Red Rock Drive
Larkspur, CO 80118-9053

1 Boeing Company
Attn: Mr. Bob Litwin
6633 Canoga Avenue
PO Box 7922 - Mail Code LA38
Canoga Park, CA 91309-7922

1 Boeing Company
Attn: Michael W. McDowell
6633 Canoga Ave. MC T038
P.O. Box 7922
Canoga Park, CA 91309-7922

1 Boeing Company
Attn: Dale Rogers
6633 Canoga Avenue
PO Box 7922 - Mail Code LA38
Canoga Park, CA 91309-7922

1 CIEMAT – Madrid
Attn: Manuel Romero Alvarez
Institudo de Energias Renovables
Avda. Complutense, 22
E-28040 Madrid
SPAIN

1 CIEMAT-PSA
Attn: Manuel J.Blanco Muriel
Apartado 22
E-04200 Tabernas (Almeria)
SPAIN

1 Edison International Corp.
Attn: Mr. Paul Lee
7103 Marcelle Street
Paramount, CA 90723

1 Ignacio Grimaldi Pastoril
Ghersa
Avda. del Puerto N 1-6
11006 Cadiz
SPAIN

1 Jose Benevente Sierra
Avda. del Puerto N 1-6
11006 Cadiz
SPAIN

1 Kearney & Associates
Attn: Mr. David W. Kearney
PO Box 2568
Vashon, WA 98070

1 KJC Operating Company
Attn: Scott D. Frier
41100 Highway 395
Boron, CA 93516-2109

1 Nagle Pumps, Inc.
Attn: Daniel L. Barth
1249 Center Avenue
Chicago Heights, IL 60411

1 Nagle Pumps, Inc.
Attn: James Nagle
1249 Center Avenue
Chicago Heights, IL 60411

1 Nexant, Inc.
Attn: Mr. William R. Gould, Jr.
45 Fremont St., 7th Floor
San Francisco, CA 94105-2210

1 Nexant, Inc.
Attn: Mr. Bruce Kelly
45 Fremont St., 7th Floor
San Francisco, CA 94105-2210

1 Nexant, Inc.
Attn: Mr. Alex Zavocio
45 Fremont St., 7th Floor
San Francisco, CA 94105-1895

1 PacifiCorp
Attn: Mr. Ian Andrews
Utah Power Generation Engineering
1407 West North Temple
Salt Lake City, UT 84140-0001

1 Pitt-Des Moines, Inc.
Attn: John C. Dewey
9719 Lincoln Village Drive, Suite 301
Sacramento, CA 95827

1 Salt River Project
Attn: Mr. Ernie Palomino
P. O. Box 52025
Mail Station ISB664
Phoenix, AZ 85072-2025

1 Tom Tracey
6922 S. Adams Way
Littleton, CO 80122

1 U. S. Department of Energy EE-11
Attn: Tommy Rueckert
1000 Independence Avenue SW
Washington, DC 20585

1 U. S. Department of Energy EE-11
Attn: Glenn Strahs
1000 Independence Avenue, SW
Washington, DC 20585

1 U. S. Department of Energy EE-11
Attn: Mr. Frank (Tex) Wilkins
1000 Independence Avenue, SW
Washington, DC 20585

1 University of Houston
Attn: Dr. Lorin Vant-Hull
Physics Department 5506
4800 Calhoun Road
Houston, TX 77204-5506

1 MS 0703 James Pacheco, 6216
1 MS 0703 Craig Tyner, 6216
1 MS 0703 Hugh Reilly, 6216
1 MS 0752 Earl Rush, 6218

1	MS 1127	Solar Tower Library
1	MS 9001	M. E. John, 8000
		Attn: R. C. Wayne, 2800, MS 9005
		J. Vitko, 8100, MS 9004
		W. J. McLean, 8300, MS 9054
		D. R. Henson, 8400, MS 9007
		P. N. Smith, 8500, MS 9002
		K. E. Washington, 8900, MS 9003
1	MS 9042	D. B. Dawson, 8725
5	MS 9402	R. W. Bradshaw, 8722
5	MS 9404	S. H. Goods, 8725
1	MS 9405	R. H. Stulen, 8700
		Attn: J. M. Hruby, 8702, MS 9401
		W. Bauer, 8704, MS 9161
		R. Q. Hwang, 8721, MS 9161
		W. R. Even, 8722, MS 9403
		J. C. F. Wang, 8723, MS 9403
		K. L. Wilson, 8724, MS 9402
		J. R. Garcia, 8725, MS 9042
		E. P. Chen, 8726, MS 9161
		J. L. Handrock, 8727, MS 9042
		M. F. Horstemeyer, 8728, MS 9042
		C. C. Henderson, 8729, MS 9401
		J. E. M. Goldsmith, 8730, MS 9055
		W. C. Replogle, 8731, MS 9409
		G. D. Kubiak, 8732, MS 9409
3	MS 9018	Central Technical Files, 8945-1
1	MS 0899	Technical Library, 9616
1	MS 9021	Classification Office, 8511/Technical Library, MS 0899, 9616
1	MS 9021	Classification Office, 8511 for DOE/OSTI